

## Determination of Phobos' Rotational Parameters by an Inertial Frame Bundle Block Adjustment

Steffi Burmeister · Konrad Willner ·  
Valentina Schmidt · Jürgen Oberst

Received: October 2017 / Accepted: date

**Abstract** A functional model for a bundle block adjustment in the inertial reference frame was developed, implemented and tested. This approach enables the determination of rotation parameters of planetary bodies on the basis of photogrammetric observations. Tests with a self-consistent synthetic data set showed that the implementation converges reliably towards the expected values of the introduced unknown parameters of the adjustment, e.g. spin pole orientation, and that it can cope with typical observational errors in the data. We applied the model to a data set of Phobos using images from the Mars Express and the Viking mission. With Phobos being in a locked rotation we computed a forced libration amplitude of  $1.14^\circ \pm 0.03^\circ$  together with a control point network of 685 points.

---

S. Burmeister  
Technische Universität Berlin  
Institute of Geodesy and Geoinformation Science  
Straße des 17. Juni 135  
10623 Berlin, Germany  
Tel.: +49-30-31423331  
Fax: +49-30-32421973  
E-mail: steffi.burmeister@tu-berlin.de

K. Willner  
German Aerospace Center (DLR)  
Institute of Planetary Research  
Rutherfordstr. 2  
12489 Berlin, Germany

V. Schmidt  
Technische Universität Berlin  
Institute of Geodesy and Geoinformation Science  
Straße des 17. Juni 135  
10623 Berlin, Germany

J. Oberst  
Technische Universität Berlin  
Institute of Geodesy and Geoinformation Science  
Straße des 17. Juni 135  
10623 Berlin, Germany

**Keywords** Adjustment techniques · Planetary Science · Rotation Elements · Reference Frame

## 1 Introduction

With the beginning of space travel there has been an ever increasing interest in exploring our Solar System. Most of the launched spacecraft carry imaging devices, and using photogrammetric stereo techniques the surface of the observed body can be reconstructed. During a first visit and mission phase to a Solar System body, efforts of geodesists will focus on the realization of reference systems. This is commonly done by establishing a control point network that requires images to be taken under specific geometric conditions (Preusker et al, 2015). Additionally, the relation between the observing sensor on the spacecraft and the body-fixed reference frame needs to be known and mathematically formulated. This includes the relative position between the observed body and the camera, as well as the relative orientation of the two reference frames to each other.

While a good estimate of the body’s rotational elements can be made from Earth observations (e.g. Gehrels, 1967; Pravec et al, 2002), smaller variations in the rotational period and the precise orientation of the body’s rotation axis, require higher resolution data like image observations from spacecraft. Rotational motion may be complex as planets are exposed to various interactions with other planetary bodies. Empirical techniques have been applied to derive rotational parameters in the past (Willner et al, 2010; Giese et al, 2011; Tajeddine et al, 2014; Oberst et al, 2014; Thomas et al, 2016). Here a plausible parameter spectrum was scanned and results of the photogrammetric stereo analysis were interpreted to determine the best fitting parameter set. In the frame of the NEAR mission, Owen et al (2001) used a method to obtain spin pole coordinates of Eros within a Least-Squares solution, which has been improved throughout the years and was also applied to data obtained by the DAWN mission targeting Vesta and Ceres (Mastrodemos et al, 2001). The multi-stage approach is based on an a priori given shape model, the construction of landmarks on the one hand and the use of Deep Space Network tracking data on the other hand; it uses repeated iteration sequences and e.g. allows to obtain rotation parameters as part of a global gravity solution (Konopliv et al, 2014).

In this study a mathematical framework for a photogrammetric bundle block adjustment is developed, which is formulated in the inertial reference frame and that allows to directly solve the collinearity equations for rotational parameters of the observed body. The term *bundle block* refers to bundles of viewing rays, formed by the lines which connect image point measurements through the focal point of a camera with the corresponding surface point. Since surface points are observed multiple times from different camera locations, a block of those bundles results and the intersections allow to determine the 3D coordinates of each surface point within certain error margins. The existing, classical, mathematical framework of the bundle block adjustment is described in Sec. 3 and the new improved method is detailed in Sec. 4. The novelty of this approach is that several rotation parameters of a planetary body can be estimated simultaneously, next to all common variables, within one bundle block adjustment. This avoids the repeated computation of adjustment results during the scanning of parameter spaces, which is especially

computational expensive when dealing with larger data sets. The implemented software was tested with a synthetic data set and proved to be robust (Sec. 5). Control point network observations for Phobos were applied to test the software with real observation data including all realistic random errors (Sec. 6). This data set appears to be especially suited as test data set, since the rotation parameters of Phobos have been studied extensively in the past (Duxbury, 1989; Oberst et al, 2014; Rambaux et al, 2012; Willner, 2009; Willner et al, 2010) and are known within well determined error margins.

## 2 Rotational Elements of Planetary Bodies

The rotational parameters of a planetary body describe the time-dependent orientation of the body-fixed rotating reference frame relative to the inertial reference frame. Rotational models of planetary bodies vary from body to body. While the spin periods of the planets are more or less random (with the notable exception of Mercury; Peale and Gold, 1965; Colombo, 1965), we find a direct and stable spin-orbit coupling for most small satellites in the Solar System.

Deviations from the uniform rotational state are induced by different perturbations leading to e.g. the forced libration, a superimposed oscillation in the mean rotational period of a body. The forced libration has been confirmed for a few moons in the Solar System (Duxbury, 1989; Tiscareno et al, 2009; Tajeddine et al, 2014). It depends on the satellite's moments of inertia, and subsequently on the lower order gravity coefficients (e.g. Borderies and Yoder, 1990; Williams et al, 2014), and is caused by the gravitational torque that a primary body exerts on its satellite. For small irregular bodies such as Phobos, the forced libration can be separated, under linear approximations, into longitudinal libration and latitudinal libration. The longitudinal libration results in an east-west oscillation of the body's surface about the principle spin axis  $Z$ . The forced libration in latitude corresponds to north-south oscillations of the surface.

Rambaux et al (2012) derived the librational spectrum from a frequency analysis of the Phobos ephemerides. The study supports our assumption that the effect of the forced libration in latitude is too small to be detected by the available observational data for Phobos. However the spatial resolution of the data and the time span covered by the Viking and Mars Express missions are sufficient to observe the predicted single forced libration in longitude as well as the precession movement. The time-independent amplitudes of these librations are rotational parameters that can be determined by an inertial frame bundle block adjustment (cf. Sec. 5 and 6).

### 2.1 General rotation model for planetary bodies

Mathematically the rotational elements are time-depending angular functions  $\alpha$ ,  $\delta$ ,  $W$  which are defined with respect to the reference epoch J2000.0 (1st January 2000, 12:00 TDB). The orientation of the spin axis at a certain time is given by the celestial coordinates  $(\alpha, \delta)$  with respect to the ICRF. Here  $\delta$  is the declination over the fundamental plane and  $\alpha$  its right ascension. The orientation of the prime meridian is specified by  $W$  according to the conventions of Archinal et al (2011),

i.e. the angle between the node at  $90^\circ + \alpha$  and the prime, measured along the body equator (cf. Fig 1 of Archinal et al, 2011).

Equations (1) show a generalized rotational model of a planetary body that undergoes a precession motion and experiences a forced libration in longitude (cf. Archinal et al, 2011). In the following  $t$  denotes the number of days past the epoch J2000.0 and  $T$  equals  $t/36525$ , the interval in Julian centuries.

$$\begin{aligned}\alpha(t) &= \alpha_0 + \alpha_1(T) + p_\alpha \sin B_1(t) \\ \delta(t) &= \delta_0 + \delta_1(T) + p_\delta \cos B_1(t) \\ W(t) &= W_0 + W_1(t) + p_W \sin B_1(t) + \theta_f\end{aligned}\tag{1}$$

In the used notation  $\alpha(0)$ ,  $\delta(0)$  denote the spin axis orientation at J2000.0, whereas  $\alpha_0$ ,  $\delta_0$  are the spherical coordinates of the mean spin axis vector w.r.t. the reference epoch. The functions  $\alpha_1$ ,  $\delta_1$  usually model long-term precessions of several thousand years which can not be covered by image data, but they can also contain more librational frequencies or completely vanish. The equations above contain a libration of the spin axis about the mean rotation axis, modeled by the function  $B_1(t)$  and its preceding amplitude factors. This motion describes a cone in the inertial frame similar to a precession cone and is further on referred to as (short-time) precession. By convention of Archinal et al (2011), the letter  $B$  depends on the planetary system considered and is typically the first letter of the primary body.  $W_1$  always contains the mean rotation period of the body and may as well include further terms (e.g. secular acceleration). Eq. 1 is integrated in the functional model of the method proposed by this paper (cf. Sec. 4), different implementations of the equation yield different rotational models.

## 2.2 Current rotation model for Phobos

It was recently pointed out, that with respect to the current ephemerides *MAR097* (Jacobson and Lainey, 2014) the rotation models of the Martian moons, as stated in Archinal et al (2011), are not in agreement with the original orbit-dependent definition (Duxbury, 2017). To model the 1:1 synchronous orbit, the prime meridian was forced to point towards the center of Mars whenever the satellite passes its pericenter or apocenter (Duxbury, 1989). Furthermore, the spin axis is assumed to be perpendicular to the orbit plane (in agreement with the IAU conventions, Archinal et al, 2011). Therefore, the rotation model depends on the used ephemerides and should be consistent with these, especially if an image analysis involves a fixed rotation model. Jacobson (2017) and Stark et al (2017) obtained resonant rotation models of Phobos as well as for Deimos with respect to *MAR097*. Both models are almost identical in their expressions. For instance, they both show a difference of  $-1.4^\circ$  in the prime meridian orientation compared to the IAU model as of September 2017. Fig. 1 shows the new rotation model by Stark et al (2017). The corresponding forced libration angle is

$$\theta_f = a_1 \sin(M_5) + a_2 \sin(M_6) + a_3 \sin(M_7)$$

where  $a_1$ ,  $a_2$ ,  $a_3$  are the forcing amplitudes that depend on the principle moments of inertia. The most dominating factor here is  $a_1$  which is known to be negative, the

other amplitudes decrease in orders of the excentricity  $\epsilon = 0.0151$  (cf. Borderies and Yoder, 1990). Hence, the forced libration in longitude can be expressed as

$$\theta_f = -p_\lambda \sin(189.6327156 + 41215158.1842005 T + 12.71192322 T^2), \quad (2)$$

with  $p_\lambda > 0$  and in agreement with the rotation model by Stark et al (2017) (cf. Fig. 1). Note, that the  $W_0$  term needs to be corrected by

$$W_0 = 35.1877444^\circ + p_\lambda \sin(189.6327156^\circ) \quad (3)$$

to achieve consistency with the prime meridian orientation at J2000.0.

For this study we used the rotation parameters provided by Stark et al (2017) as well as – for reasons of comparison – the previous IAU model (Archinal et al, 2011).

|   |  |
|---|--|
| $\alpha = 317.67071657^\circ - 0.10844326^\circ T$<br>$-1.78428399^\circ \sin(M1) + 0.02212824^\circ \sin(M2)$<br>$-0.01028251^\circ \sin(M3) - 0.00475595^\circ \sin(M4)$<br>$\delta = 52.88627266^\circ - 0.06134706^\circ T$<br>$-1.07516537^\circ \cos(M1) + 0.00668626^\circ \cos(M2)$<br>$-0.00648740^\circ \cos(M3) + 0.00281576^\circ \cos(M4)$<br>$W = 35.18774440^\circ + 1128.84475928^\circ d + 12.72192797^\circ T^2$<br>$+1.42421769^\circ \sin(M1) - 0.02273783^\circ \sin(M2)$<br>$+0.00410711^\circ \sin(M3) + 0.00631964^\circ \sin(M4).$ | $M1 = 190.72646643^\circ + 15917.10818695^\circ T$<br>$M2 = 21.46892470^\circ + 31834.27934054^\circ T$<br>$M3 = 332.86082793^\circ + 19139.89694742^\circ T$<br>$M4 = 394.93256437^\circ + 38280.79631835^\circ T$<br>$M5 = 189.63271560^\circ + 41215158.18420050^\circ T$<br>$+ 12.71192322^\circ T^2$<br>$M6 = 19.26538605^\circ + 82430316.36864280^\circ T$<br>$+ 25.42412173^\circ T^2$<br>$M7 = 208.89882434^\circ + 123645474.54466790^\circ T$<br>$+ 38.13293168^\circ T^2.$ |
|---|--|

**Fig. 1** Resonant rotation model of Phobos by Stark et al (2017),  $d$  are days passed since J2000.0 and  $T = d/36525$ . The functions  $M_5$ ,  $M_6$  and  $M_7$  specify the frequencies of the forced libration given as  $a_1 \sin(M_5) + a_2 \sin(M_6) + a_3 \sin(M_7)$  with  $a_1, a_2, a_3$  being the forcing amplitudes that depend on the principle moments of inertia.

### 3 Classical Functional Model

A control point network is computed in the body-fixed frame. Therefor, exterior and interior orientation parameters of the camera are needed as input. The interior orientation parameters – focal length, principle point coordinates and image distortion – are usually calibrated during dedicated pre-flight and in-flight campaigns (Oberst et al, 2008), they remained fix within this study. In the common approach, the exterior orientation data of the camera – position and pointing data – are required with respect to the body-fixed reference frame. These parameters, usually available as predicted or reconstructed data with respect to the inertial reference frame, are provided by the space operation centers (e.g. ESOC) and are converted into the body-fixed frame for the application of the bundle block adjustment. This transformation involves a model of the body’s state (the ephemerides) and orientation with respect to the inertial space (cf. Eq. 1).

Equation (4) shows the relation between camera coordinates  $(x, y, -f)_C$  of the observed image points (where  $f$  is the focal length of the camera), the camera position  $(X_0, Y_0, Z_0)_B$ , and object point coordinates  $(X, Y, Z)_B$  upon which the classical bundle block adjustment is based. The subscript  $B$  denotes that these

values are expressed in the body-fixed coordinate frame and  $_C$  refers to the camera reference frame (Albertz and Wiggenhagen, 2009):

$$\begin{pmatrix} X \\ Y \\ Z \end{pmatrix}_B = m R_{CB} \begin{pmatrix} x \\ y \\ -f \end{pmatrix}_C + \begin{pmatrix} X_0 \\ Y_0 \\ Z_0 \end{pmatrix}_B . \quad (4)$$

The matrix  $R_{CB}$  is a rotation matrix and transforms the observed vector  $(x, y, -f)_C$  from the camera coordinate frame into the body-fixed frame. It is related to the time stamp of the image which contains the observation, and hence varies over a sequence of images. All vectors are given in meters here. The factor  $m$  is a real number which scales the transformed vector depending on the distance to the surface point. Depending on the actual definition of the camera reference system, the observed image point coordinates might need to be transformed in order to satisfy Eq. (4).

#### 4 Adapted Functional Model

The introduced matrix  $R_{CB}$  is derived by subsequently orienting the camera frame first with respect to the inertial frame and then with respect to the body-fixed frame. This is accomplished by applying first the exterior information for the camera and then the orientation model for the body that is observed, and can be denoted as

$$R_{CB} = R_B \cdot R_C^T . \quad (5)$$

$R_C^T$  solely depends on the attitude information of the camera at image time and represents the camera frame to inertial frame transformation.  $R_B$  provides the rotation from the inertial frame to the body-fixed frame at this time (probably corrected for light-time travel). The matrix is build by three subsequent rotations about the rotational elements  $\alpha$ ,  $\delta$  and  $W$  (cf. Archinal et al, 2011):

$$R_B = R_3(W)R_1\left(\frac{\pi}{2} - \delta\right)R_3\left(\frac{\pi}{2} + \alpha\right) , \quad (6)$$

where  $R_1$  and  $R_3$  are given by

$$R_1(\theta) = \begin{pmatrix} 1 & 0 & 0 \\ 0 & \cos(\theta) & \sin(\theta) \\ 0 & -\sin(\theta) & \cos(\theta) \end{pmatrix} , \quad R_3(\theta) = \begin{pmatrix} \cos(\theta) & \sin(\theta) & 0 \\ -\sin(\theta) & \cos(\theta) & 0 \\ 0 & 0 & 1 \end{pmatrix}$$

and denote the rotation about the X and Z axes of the transforming coordinate frame, respectively. The elements of  $R_B$  are linear combinations of trigonometric functions whose arguments are the rotational elements. Substituting  $R_{CB}$  in Eq. (4) with Eq. (5), leads to the following equation:

$$\begin{pmatrix} X \\ Y \\ Z \end{pmatrix}_B = m R_B R_C^T \begin{pmatrix} x \\ y \\ -f \end{pmatrix}_C + R_B \begin{pmatrix} X_0 \\ Y_0 \\ Z_0 \end{pmatrix}_{ICRF} . \quad (7)$$

The subscript  $ICRF$  denotes that the camera position vector is expressed with respect to the ICRF. Hence, the coordinates themselves are no longer linked with

the orientation of the observed body. Furthermore Eq. (7) can be solved for the body's rotation parameters as these are now accessible via the entries of  $R_B$ . The parametric least squares adjustment, that is applied here, requires a representation of the observations – the image coordinates  $x, y$  – as function of the unknown parameters. Equation (7) can be re-arranged to isolate the observations on the left hand side of the equation.

$$\begin{pmatrix} x \\ y \\ -f \end{pmatrix}_C = \frac{1}{m} R_C \left( R_B^T \begin{pmatrix} X \\ Y \\ Z \end{pmatrix}_B - \begin{pmatrix} X_0 \\ Y_0 \\ Z_0 \end{pmatrix}_{ICRF} \right).$$

The right hand side of the equation is now substituted with the vector  $(X', Y', Z')$ . Since  $f$  is the constant focal length of the camera, from this equation the known form of the collinearity equations can be obtained

$$x = -f \frac{X'}{Z'} \quad , \quad y = -f \frac{Y'}{Z'} . \quad (8)$$

Now  $X', Y'$  and  $Z'$  directly depend on the rotational elements of the body and the partial derivatives over these can be derived. The vector  $X', Y', Z'$  further depends on the other unknown parameters that are the body-fixed coordinates of the control points as well as the exterior orientation of the camera. The latter parameters are also included as observations to constrain the datum of the entire framework. Note, that  $m$  has been canceled out by deviding  $X'/Z'$  resp.  $Y'/Z'$ , which reduces the number of unknown parameters for each image by one. More detailed information about the functional model, e.g. the computation of the partial derivatives are given in (Burmeister, 2017, chap. 3).

## 5 Data Simulation and Model Testing

To test and evaluate the implemented method a synthetic data set was created. An existing control point network (CPN) of Phobos (Willner et al, 2010) and the related body-fixed position and attitude data of the camera were used to calculate image coordinates, based on Eq. (8). The CPN consists of 679 points that were observed 5 times on average while observations were distributed across 73 images. Viking image observations were obtained during a continuous block of 10 days in Feb. 1977 whereas Mars Express data covers the time between 2004 and 2007. By applying the rotational model of Phobos as stated in Archinal et al (2011), a self-consistent synthetic data set with inertial camera positions and pointing angles with respect to the ICRF was derived. Here, the pointing angles have been obtained from the matrix  $R_C^T$  after re-arranging Eq. (5).

The meanwhile outdated model included a precession ellipse (in ICRF coordinates) where the parameters  $p_\alpha = 1.79$ ,  $p_\delta = 1.08$ ,  $p_W = 1.42$  satisfied the following functional dependence

$$p_\delta = p_\alpha \cos(\delta_0), \quad p_W = p_\alpha \sin(\delta_0), \quad (9)$$

which is used in the adjustment to only solve for one of the three parameters. This relation typically holds for the precession and nutation triples in Archinal et al

(2011), but it is no longer valid for the most recent rotation models for Phobos and Deimos (cf. Sec. 6).

To identify possible weak points of the software and functional model of the least squares adjustment, tests based on the synthetic data set were performed by varying initial values for different parameters at a time. It was then tested if the solution for these parameters was converging towards the correct predicted value.

In a first step, different starting values were used for the parameters  $p_\lambda$ ,  $p_\alpha$ ,  $\alpha_0$ ,  $\delta_0$ , deviating from the ones used to derive the synthetic data set, but all other involved parameters were not afflicted with errors. The adjusted values for the rotational parameters show very small reconstruction errors, confirming that the implemented approach is suitable to solve directly for the rotational parameters. In Table 1, eight scenarios are summarized: three examples for  $p_\lambda$  (Case 1), two examples for a joint determination of  $p_\lambda$ ,  $p_\alpha$  (Case 2) and three scenarios for the mean pole axis orientation  $\alpha_0$ ,  $\delta_0$  (Case 3). The maximal reconstruction error is in the order of  $0.00054^\circ$  and related to the polar precession amplitude. It would induce a surface displacement of only a few centimeters. All other scenarios led to reconstruction of the varied parameters within  $\pm 0.0003^\circ$ . The error of the libration amplitude was two to four times smaller than the errors of rotation parameters related to the pole axis orientation.

**Table 1** Different adjustment cases for the simulation with falsified rotational parameters as start values for the adjustment. Position and attitude values were not afflicted with errors. Case 1 and 3 were tested with three different error magnitudes for the forced libration amplitude  $p_\lambda$  resp. the mean pole axis orientation ( $\alpha_0$ ,  $\delta_0$ ), case 2 was tested with two different error magnitudes for the precession cone parameter  $p_\alpha$  together with  $p_\lambda$ ;  $\epsilon = 10^{-4}$  degree.

| Case   | Par.        | Added Errors |              |              | Max. Error<br>after Adj. | Test<br>Scenarios |
|--------|-------------|--------------|--------------|--------------|--------------------------|-------------------|
|        |             | 1.           | 2.           | 3.           |                          |                   |
| Case 1 | $p_\lambda$ | $-4.2^\circ$ | $+0.8^\circ$ | $+1.8^\circ$ | $< 1.2 \epsilon$         | 3                 |
| Case 2 | $p_\alpha$  | $-1.8^\circ$ | $-0.8^\circ$ | –            | $< 5.4 \epsilon$         | 2                 |
|        | $p_\lambda$ | $+0.8^\circ$ | $+0.9^\circ$ | –            | $< 1.0 \epsilon$         |                   |
| Case 3 | $\alpha_0$  | $-0.9^\circ$ | $-2.7^\circ$ | $-17^\circ$  | $< 2.4 \epsilon$         | 3                 |
|        | $\delta_0$  | $-1.0^\circ$ | $+2.1^\circ$ | $-13^\circ$  | $< 3.0 \epsilon$         |                   |

To design more realistic test scenarios, individually defined errors were added to the pointing and/or position information of the camera in a second step. The errors with a given upper limit resulted from a combination of pseudo-random uniform distribution and human random choice, and were then assigned manually and in random order (by human choice again) to each camera orientation. Different test classes were prepared. In one class only the camera pointing information were afflicted with errors ranging up to  $\pm 0.9^\circ$ , and in another class only camera position information were varied with random numbers within the limits of  $\pm 1200$  m (see Table 2 for individual settings). A third test class combines pointing and positional errors of the camera in different pairs of magnitudes. This way 15 data sets of falsified a priori orientation parameters were created in total. The maximal errors have been chosen higher than typical errors of modern tracking and orbit determination methods let expect, especially high enough to clearly exceed the

error margins of the orientation data we will use in Sec. 6 where we apply the adjustment to real observational data.

**Table 2** Different test classes for the simulation containing the camera orientation data with different errors on position and pointing data

| Class   | Pointing-Errors                                | Positions-Errors                                       | Data Sets |
|---------|--|--|-----------|
| Class 1 | $\pm 0.05^\circ, \pm 0.5^\circ, \pm 0.9^\circ$ | none   | 3         |
| Class 2 | none   | $\pm 15\text{ m}, \pm 300\text{ m}, \pm 1200\text{ m}$ | 3         |
| Class 3 | $\pm 0.05^\circ, \pm 0.5^\circ, \pm 0.9^\circ$ | $\pm 15\text{ m}, \pm 300\text{ m}, \pm 1200\text{ m}$ | 9         |

To complete the test scenario, the rotational parameters were varied as before (see Table 1), and the eight adjustments were repeated for all 15 data sets with different stochastic models. In all performed adjustments all of the classical unknown parameters, related to position/pointing of the camera and the control point coordinates, were estimated together – no matter if they were afflicted with errors or not. Assuming a very high accuracy in the stochastic model for some of the parameters results in negligibly small changes of the initial values. The applied stochastic models were using the real magnitude of the added errors and, in some cases, higher errors in additional test runs. The adjustments do not converge exactly towards the simulated values, the remaining difference is called the reconstruction error below. It was largest when the orientation data of class 3 was used which combines errors of  $\pm 1200\text{ m}$  in the camera position and  $\pm 0.9^\circ$  in the camera pointing. We will call this the case of the largest errors below. The results of the more than 100 test runs can be summoned as follows:

- The topography, i.e. the 3D coordinates of the control points, could be reconstructed within the pixel resolution of the images in all of the test runs. The difference to the predefined coordinates was  $\varnothing 17.5\text{ m}$  (max. 37 m) in the case with the largest errors. In all other cases the CPN’s reconstruction error ranges between 0.05 m and 8 m in average.
- The forced libration amplitude could be reconstructed within two to six iterations up to an accuracy level between  $\pm 0.0002^\circ$  and  $\pm 0.0026^\circ$  depending on the magnitude of the errors of the different parameters. In the case of the largest errors, the mean pole axis orientation shows remaining errors of  $-0.01^\circ$  for  $\alpha_0$  and  $-0.022^\circ$  for  $\delta_0$ .
- When the positions were not afflicted with errors, the pointing data could be reconstructed within less than  $\pm 0.002^\circ$ . In test cases with combined errors, the maximal reconstruction error was about  $\pm 0.01^\circ$ .
- The coordinates of the control points could successfully be reconstructed despite the remaining errors on the camera positions. The positions were not reconstructed to their exact value. Instead the incorrect camera positioning was compensated by larger corrections on the camera pointing. This can be expected as the camera pointing has a much stronger influence on the coordinates of the control points due to the large distance to the object. Given the accuracy of the rotational parameters, we conclude that the position errors are fully compensated by the pointing corrections. The only possible ex-

ception is test case 3 scenario 3 with the largest errors on the orientation data, since here the reconstruction accuracy decreases to  $0.022^\circ$  for  $\delta_0$ . But it is more likely that the large pointing error of  $\pm 0.9^\circ$  is responsible for the larger deviation and should therefore mark the upper limit of acceptable pointing errors.

The tests with the synthetic data set showed that the algorithm is functional and that for data sets with errors in the order of  $\pm 300$  meters in position and  $\pm 0.5$  degrees in orientation a very accurate reconstruction (below  $\pm 0.003^\circ$ ) of rotational parameters was achieved. The mean error of control point coordinates stayed well below the pixel resolution of the images. Applied to the camera orientation data of  $\pm 1200$  m and  $\pm 0.9^\circ$ , the control point coordinates and forced libration amplitude could still be reconstructed to a satisfactory level. However, the solution for pole axis orientation was only accurate to  $\pm 0.022^\circ$ . It was demonstrated that the initial values for the rotational parameters may be rather inaccurate in comparison to the final solution. Offsets in the pole axis orientation of  $17^\circ$  in right ascension and  $13^\circ$  in declination as well as a  $4^\circ$  difference in the forced libration amplitude were reconstructed successfully.

In all test cases with the synthetic data set the image point observations were not afflicted with errors. This is considered less critical as during the adjustment outliers, such as wrong point measurements, are removed and remaining measurement errors are estimated to be in the order of  $\pm 1$  pixel. Propagating such an error of  $\pm 17$  m per observation (cf. Table 3) only to the forced libration amplitude would result in an additional error for the forced libration of  $\pm 0.05$  degrees. But since errors are compensated by several variables within the adjustment, the influence of the measurement error is much smaller – w.r.t. this data set not more than  $0.013^\circ$ . This is not an absolute quantity since the error propagation depends on the spacecraft distance (hence the pixel resolution) and is as well proportional to the size of the target body.

## 6 Rotational Parameters and a Control Point Solution for Phobos

After testing the implemented approach with a synthetic data set that provides the full control of the parameters, a real scenario was considered. Existing control point observations for Phobos were used and a solution for the longitudinal forced libration was estimated. The image point observations are essentially the same as Willner et al (2010) used for their study (cf. Sec. 6.2). For the adjustment, the Phobos-centered camera vectors (cf. Eq 7) were obtained using the *MAR097* ephemerides (Jacobson and Lainey, 2014) and the Mars Express orbit provided by ESOC while the new rotational model by Stark et al (2017) was applied to describe the orientation of Phobos w.r.t. the inertial reference frame. Additional adjustments using previous ephemerides *MAR080* (Jacobson, 2008) and the rotation model from Archinal et al (2011) were performed in order to show the dependency of the result to the chosen orbit and body rotation model.

## 6.1 Observations

Image points were observed in images obtained by the NASA Viking Orbiter 1 (VO1) mission, operating from June 1976 and August 1980, and ESA's Mars Express (MEX) mission. The data set includes observations in 19 VO1 images. The majority of the VO1 images was taken during the early encounter phase at an average distance of 460 km, and two of the images are captured in late 1977 at 1840 km and 3100 km distance. The Viking Imaging System (VIS) consisted of two identical cameras, VIS A and VIS B. One image of VIS B and 18 images of VIS A were used for image point observations. The positioning and attitude information of the Viking orbiters is known to be defective. Zeitler and Oberst (1999) report, that the efforts in improving the positional information of the Viking orbiters by Konopliv and Sjogren (1995) led to orbits which are accurate to a few hundred meters. The pointing was reported to be accurate within  $\pm 0.5^\circ$ .

Two and a half decades later, on 25th December 2003, MEX entered into a highly elliptic polar Mars orbit reaching beyond the orbit of Phobos at its apoapsis (Jaumann et al, 2007; Witasse et al, 2014). While MEX continues to operate, the Super Resolution Channel (SRC) of the High Resolution Stereo Camera on-board the Mars Express spacecraft is used to observe Phobos on a regular basis from distances of less than 5000 km. Willner et al (2010) selected 53 frame images of the SRC to observe image point coordinates, taken at an average distance of 1887 km with respect to Phobos' center of mass. Pischel and Zegers (2009) estimate the uncertainty of MEX positions provided by ESOC to be in the order of  $\pm 200$  m on average and an uncertainty for the spacecraft pointing in the order of  $\pm 0.01$  degrees (covering data until 31. Dec. 2006). Pasewaldt et al (2015) who analyzed SRC images up to July 2011 confirm the pointing errors and state the MEX position uncertainties with  $\pm 224$  m. Rosenblatt et al (2008) obtained MEX orbits at the Royal Observatory of Belgium with accuracies of 20-25 m on average (sometimes up to 300 m) using data of the period 2004-2006. The latter orbits are not considered in this study since the period does not cover the whole time span of the images used here. Table 3 provides a summary of the observational data.

**Table 3** The nominal ground distance (km), assuming a radius of 11 km, and the resulting ground resolution (m) of Viking and MEX images. The average resolution of all 72 images together is 17 m.

|                     | Viking (VIS)    | MEX (SRC)              |
|---------------------|-----------------|------------------------|
| Pixel Size          | 0.01176 mm      | 0.009 mm               |
| Focal Length        | 474.610 mm      | 984.76 mm <sup>a</sup> |
| Positional Accuracy | $\pm 1$ km      | $\pm 224$ m            |
| Pointing Accuracy   | $\pm 0.5^\circ$ | $\pm 0.01^\circ$       |
| Average Distance    | 674 km          | 1877 km                |
| Average Resolution  | 16.68 m         | 17.12 m                |
| Number of Images    | 19              | 53                     |
| Time Span           | Feb 1977        | May 2004 - Aug 2007    |

<sup>a</sup> In flight calibrated (Duxbury et al, 2011)

The observations comprise 8010 image point measurements of 689 control points, distributed over the 19 Viking Orbiter and 53 Mars Express images.

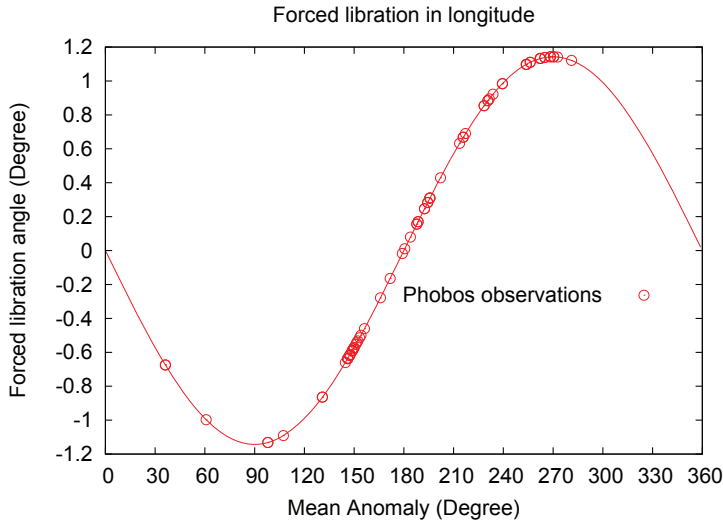


**Fig. 2** The forced libration in longitude (FL) through one orbit of Phobos. The plot shows the function  $-1.143 \sin(189.63271560 + 41215158.1842005 T + 12.71192322 T^2)$ . The circles indicate Phobos' mean anomaly at the times of image observations. Between 90 degrees and 270 degrees there is an almost homogeneous distribution of observation points.

## 6.2 Adjustment Results

The 3D coordinates of the control points in the body fixed frame are unknown parameters in all cases. Selected parameters of the rotation model (cf. Table 5) were introduced as unknown parameters whereas all remaining rotation parameters were kept fix in the adjustment. The parameter set of observations comprises the image point coordinates (in terms of fixed observations) as well as the position and attitude information of the camera (as observed unknowns). It is assumed that the internal camera geometries are well known and are thus introduced as a constant parameter set (Oberst et al, 2008; Duxbury et al, 2011; Klaasen et al, 1977). The used camera orientation parameters rely on the Mars Express orbit and attitude data provided by ESOC and are available as SPICE kernel data (Acton, 1996). Table 4 shows all involved kernels.

We note that the center of figure was not explicitly observed and introduced as a control point during this analysis. Hence, the resulting 3D-coordinates are initially not tied to the center of figure of Phobos. Instead the control point reduction relies on the computed position of Phobos from the orbit prediction model.

The accuracies for the different observations, defining their weight in the adjustment, were chosen according to the current best knowledge (cf. Table 3). The initial observations of the exterior camera orientation parameters have been

**Table 4** SPICE kernels used to obtain camera orientation

| Type        | Kernel                   | Application                           |
|-------------|--------------------------|---------------------------------------|
| Position    | de421.bsp                | Planetary ephemerides                 |
|             | mex.all.bsp <sup>a</sup> | MEX s/c position                      |
|             | MAR097.BSP               | Martian moon ephemerides              |
|             | vo1_rcon.bsp             | VO s/c position                       |
| Orientation | mex.all.bc <sup>b</sup>  | MEX s/c orientation                   |
|             | vo1_sedr_ck2.bc          | VO s/c orientation                    |
| Instrument  | MEX_HRSC_V04.TI          | HRSC camera parameter                 |
|             | vo1_visa_v20.ti          | VO1 camera A parameter                |
|             | vo1_visb_v20.ti          | VO1 camera B parameter                |
| Frame       | MEX_V11.TF               | MEX frame definitions                 |
|             | vo1_v10.tf               | VO1 frame definitions                 |
| Time        | NAIF0010.TLS             | Leap-seconds (for time conversion)    |
|             | MEX_130305_STEP.TSC      | MEX spacecraft clock correction terms |
|             | vo1_fict.tsc             | VO1 spacecraft clock correction terms |

<sup>a</sup> contains all predicted and reconstructed ephemerides for MEX (updated monthly)

<sup>b</sup> summarizes all predicted pointing information for MEX

**Table 5** Adjustment results for the forced libration amplitude  $p_\lambda$  depending on the used ephemeris and a priori rotation model. Based on the initial values ( $p_0$ ) the adjustment converged to the adjusted values ( $p_{adj.}$ ) with their associated error  $\sigma$ ,  $\Delta p = p_0 - p_{adj.}$ . Case 5 is a joint adjustment where the mean pole axis vector ( $\alpha_0, \delta_0$ ) is estimated, too.

| Ephemerides | Rot. Model                       | Adj.           | $p_0$          | $p_{adj}$       | $\Delta p$     | $\sigma$           |
|-------------|----------------------------------|----------------|----------------|-----------------|----------------|--------------------|
| MAR097      | Stark et al<br>(2017)            | 1) $p_\lambda$ | $1.2^\circ$    | $1.143^\circ$   | $+0.057^\circ$ | $\pm 0.0253^\circ$ |
|             |                                  | 2) $p_\lambda$ | $0.0^\circ$    | $1.143^\circ$   | $+1.143^\circ$ | $\pm 0.0251^\circ$ |
| MAR080      | Stark et al<br>(2017)            | 3) $p_\lambda$ | $1.2^\circ$    | $1.031^\circ$   | $+0.169^\circ$ | $\pm 0.0241^\circ$ |
|             |                                  | 4) $p_\lambda$ | $0^\circ$      | $1.028^\circ$   | $+1.028^\circ$ | $\pm 0.0239^\circ$ |
| MAR097      | IAU<br>(Archinal et al,<br>2011) | $p_\lambda$    | $0.78^\circ$   | $1.133^\circ$   | $+0.353^\circ$ | $\pm 0.0256^\circ$ |
|             |                                  | 5) $\alpha_0$  | $317.68^\circ$ | $317.655^\circ$ | $-0.025^\circ$ | $\pm 0.0253^\circ$ |
|             |                                  | $\delta_0$     | $52.9^\circ$   | $52.885^\circ$  | $-0.015^\circ$ | $\pm 0.0192^\circ$ |

weighted by applying a simple (diagonal) stochastic model according to the accuracies provided in Table 3. The accuracy of the observed image point coordinates was set to one pixel which relates to an uncertainty of 0.009 mm for points observed in SRC images and 0.01176 mm for points observed in VO1 images.

Two adjustments models are distinguished depending on the selected rotation parameters. At first, only the forced libration amplitude  $p_\lambda$  was introduced as unknown rotation parameter. As stated in Sec. 2, the expression for the prime meridian orientation  $W$  in the model of Stark et al (2017) does not yet include the forced libration angle. Since the forced libration amplitude is expected to be in the order of 1 degree, its effect is much stronger than changes in the other rotation parameters, which are assumed to be accurate to  $\pm 0.01^\circ$  w.r.t. J2000.0 (Archinal et al, 2011). With different initial values ( $1.2^\circ$ ,  $0^\circ$ ) the solution converged to  $p_\lambda = 1.143^\circ (\pm 0.03^\circ)$  in all cases (cf. Table 5). This solution is based on the current ephemerides and is in agreement with previous results  $1.24^\circ \pm 0.15^\circ$  (Willner et al, 2010),  $1.09^\circ \pm 0.09^\circ$  (Oberst et al, 2014) as well as  $0.8^\circ \pm 0.4$  Duxbury (1989).

The amplitude of  $1.2^\circ$ , adopted by Jacobson and Lainey (2014) in the ephemeris computation, falls in the  $2\sigma$  range of our solution. The corresponding  $W_0$  term for the prime meridian at J2000.0 is

$$W_0 = 34.99648425^\circ \quad (p_\lambda = 1.143^\circ). \quad (10)$$

We then repeated the first adjustment model with respect to the previous ephemeris release *MAR080* (Jacobson, 2008) and obtained  $p_\lambda = 1.03^\circ \pm 0.024^\circ$ . The result varies by  $0.11^\circ$ , it agrees with the value that has been obtained by (Jacobson, 2010) and clearly shows the dependency on the orbit model. Contrary to the first case a slight dependency on the a priori value of  $p_\lambda$  can be noticed here, since the results of adjustment 3) and 4) differ by 0.003 degree.

With the second model, the pole axis orientation and the forced libration were obtained during a joint adjustment. To estimate the dependency of the resulting  $p_\lambda$  value on the a priori rotation model, here the IAU rotation model (Archinal et al, 2011) was used together with *MAR097* ephemerides (Jacobson and Lainey, 2014). The resulting forced libration amplitude  $p_\lambda = 1.133^\circ \pm 0.024$  is consistent with the first result ( $p_\lambda = 1.143^\circ \pm 0.0253$ ). The difference of  $0.01^\circ$  is within the error bounds of both solutions and relates to a small surface displacement of a few meters. The result for  $\alpha_0$  differs by  $\sigma = 0.015^\circ$  from the current value of Stark et al (2017) while  $\delta_0$  only differs by  $0.001^\circ$ . According to our result the assumption, that Phobos' rotational axis is indeed perpendicular to its orbit, is confirmed with  $2\sigma$  accuracy and strong confidence on the assumed mean declination. May be a more accurate solution for  $\alpha_0$  can be obtained, if constraints are put on the selected rotational parameters which has not been tried here.

The obtained control point network (CPN) consists of 685 points with an average intersection error of 13 m. This is well below the average pixel resolution of all images (Table 3). The distribution of the control points with associated intersection errors are shown in Figure 3. About 46 % of the control points have errors of less than  $\pm 10 m$  while 49 % have an error which ranges between  $\pm 10 m$  and  $\pm 30 m$ . Only about 5 % have a larger uncertainty than  $\pm 30 m$ . Compared to the CPN obtained by Willner et al (2010) the new approach produced a CPN solution with 20 more points and smaller intersection errors.

The derived 685 control points were triangulated, rendered and illuminated to display the overall shape and major topographic features for visual control (Fig. 4). The large Stickney crater on the western hemisphere (Fig. 4a) is well recognizable.

## 7 Summary and Conclusion

We have introduced a new block adjustment technique operating in inertial frame coordinates, which allows to solve directly and effectively for rotational parameters. Rotational parameters can be obtained significantly faster than in the traditional method of scanning the parameter spectrum. Furthermore, a decoupling of the spacecraft position and orientation from the orientation model of the observed body is achieved as the functional model allows a change in the bodies rotation without influencing the spacecraft's exterior information.

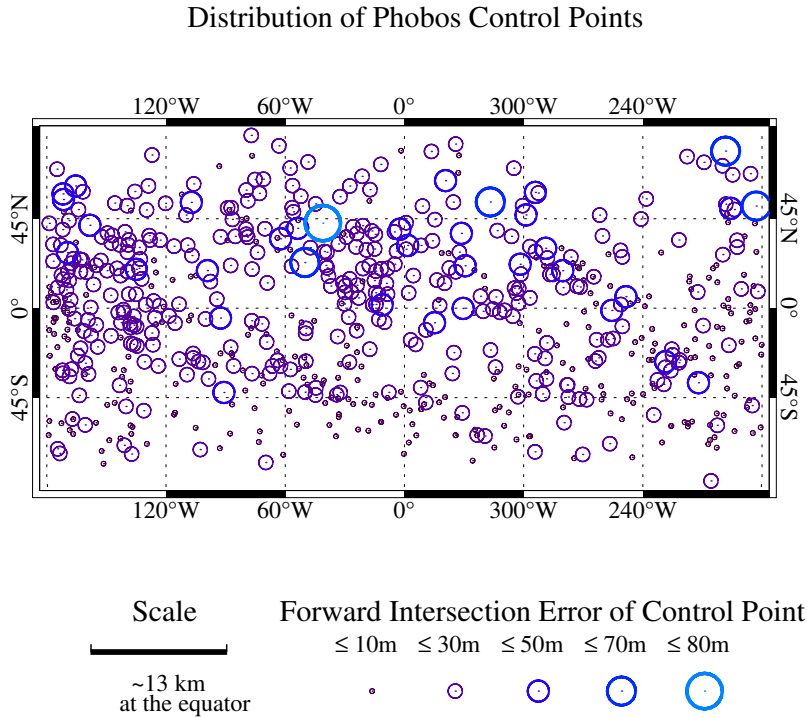
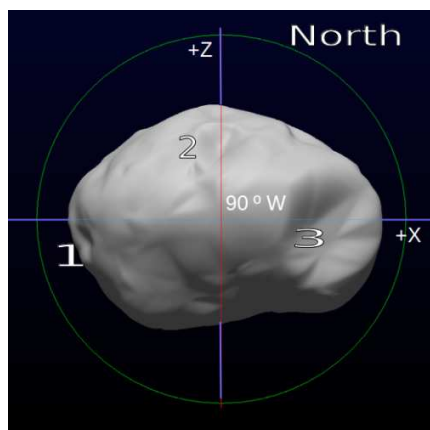


**Fig. 3** Distribution of control points on Phobos (projected on the unit sphere) with forward intersection errors, ranging from 10 m to 80 m. The majority of points (95 %) has errors below 30 m.

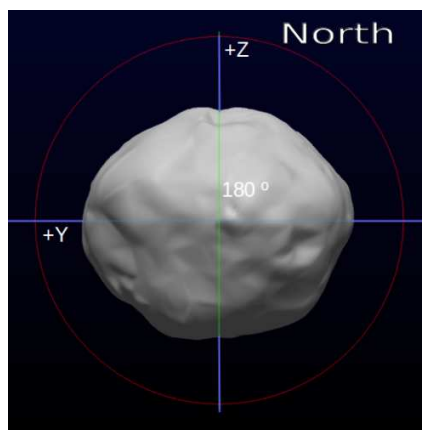
The method was tested with a synthetic data set that allowed full control of the errors on all observed quantities. An adjustment starting with falsified information converged reliably towards the expected values within very small formal error margins (at the  $0.0004^\circ$  level). The defined topography could be successfully reconstructed within the average pixel resolution up to pointing errors of  $\pm 0.9^\circ$  and camera position errors of  $\pm 1200$  m.

The method has been applied on a data set of Phobos image point observations. The (longitudinal) forced libration amplitude was determined to be  $1.143^\circ$  ( $\pm 0.025^\circ$ ), based on the current ephemerides (Jacobson and Lainey, 2014) and rotation model by Stark et al (2017). This is different to previous results but within the reported error bars. Within this adjustment we also updated the corresponding  $W_0$  term respecting the dependency of  $p_\lambda$  and the prime meridian orientation at the reference epoch – the new value is  $W_0 = 34.99648425^\circ$ .

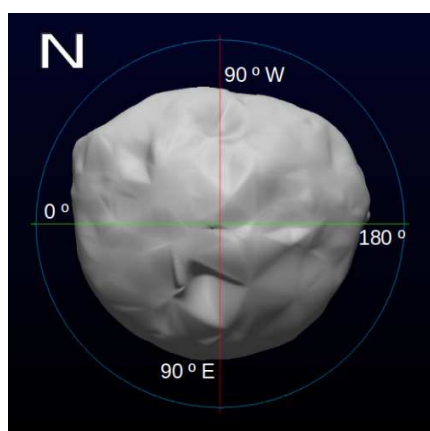
It was further demonstrated that the result of the libration amplitude depends on the used ephemerides and on the consistency of orbit model and rotation model. A difference of  $0.11^\circ$  between the current ephemerides Jacobson and Lainey (2014) and the previous release Jacobson (2008) has been noticed which corresponds to a displacement of about 30 m on the equator of Phobos. Using the former rotation model for Phobos and current orbital model, the mean pole axis orientation could



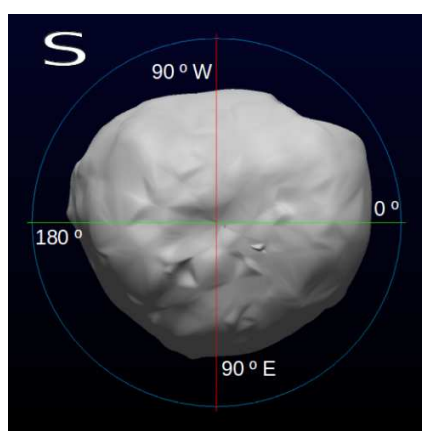
**a** Western hemisphere showing the craters 1) Todd, 2) Drunlo and 3) Stickney



**b** View centered at  $180^\circ$  (vertical) and equator (horizontal)



**c** Northern hemisphere with four longitudes ( $0^\circ, 90^\circ E, 180^\circ E, 90^\circ W$ )



**d** Southern hemisphere with four longitudes ( $0^\circ, 90^\circ W, 180^\circ E, 90^\circ E$ )

**Fig. 4** Reconstructed shape of Phobos from 685 control points, triangulated and rendered with simulated light source. The four different perspectives are projections into fundamental planes with the view centered at the third axis. +X contains the prime meridian, +Y  $90^\circ E$  and +Z the northern +pole.

be improved in agreement with the current rotation model (Stark et al, 2017) and the amplitude of the forced libration angle shows a difference of  $0.01^\circ$  w.r.t. our main result. The difference in the amplitude relates to meter changes on the surface and is not significant.

Determination of correlated rotation parameters within one adjustment requires the introduction of a covariance matrix to model the correlations. This was not required in order to determine the librational amplitude but is considered for future works.

## 8 Outlook

The implemented adjustment in the inertial reference frame has two prime characteristics that distinguishes it from other implementations. For one it is possible to solve for rotational parameters. Though not demonstrated in this work, theoretically it should be possible to solve also for the mean rotation rate, precession period or acceleration. It has not been tried yet whether or not it is possible to include all major rotation parameters together into the set of unknowns, but it will be assessed in future. Secondly the implementation is optimized for very large data sets (i.e. MESSENGERS Mercury observations) by making use of sparse matrix and iterative inversion techniques (Burmeister, 2017). The rotation model of a body is of great interest since it reveals interactions with other bodies and can be used to infer its moments of inertia. Thus the rotational model provides further constraints to the interior structure of a body.

Several missions collected a data base sufficient to apply the introduced approach. First of all, the data of the Rosetta mission which investigated Comet 67P/Churyumov-Gerasimenko, would be of great interest as a precession has been confirmed already (Preusker et al, 2015) and other rotation effects might be detectable. The DAWN mission would be another example with its visits to Vesta and Ceres delivering enough data to apply the bundle adjustment in the inertial space and to refine rotation models for the asteroid and dwarf planet.

Image data of the satellites of Saturn, obtained by Voyager and Cassini, also provide a host of opportunities to study the rotational motion of bodies like Mimas, Enceladus, and Epimetheus which are known to undergo forced librations (Tiscareno et al, 2009; Tajeddine et al, 2014).

**Acknowledgements** We thank the HRSC Experiment team at DLR, Institute of Planetary Research, Berlin, and at Freie Universität Berlin, the HRSC Science Team, as well as the Mars Express Project teams at ESTEC, ESOC, and ESAC for their successful planning and acquisition of data as well as for making processed data available to the HRSC team. S. Burmeister was supported by the Deutsche Forschungsgemeinschaft (DFG) under FKZ OB 124/11-1 and FKZ OB 124/14-1.

## References

- Acton CH (1996) Ancillary data services of NASA's Navigation and Ancillary Information Facility. *Planetary and Space Science* 44:65–70
- Albertz J, Wiggenhagen M (2009) *Taschenbuch zur Photogrammetrie und Fernerkundung / Guide for Photogrammetry and Remote Sensing*, 5th edn. Wichmann
- Archinal BA, A'Hearn MF, Bowell E, Conrad A, Consolmagno GJ, Courtin R, Williams IP, et al (2011) Report of the IAU Working Group on Cartographic Coordinates and Rotational Elements: 2009. *Celestial Mechanics and Dynamical Astronomy* 109:101–135
- Borderies N, Yoder CF (1990) Phobos' gravity field and its influence on its orbit and physical librations. *Astronomy and Astrophysics* 233:235–251
- Burmeister S (2017) Determining rotational elements of planetary bodies. PhD thesis, Technische Universität Berlin, DOI 10.14279/depositonce-5796

- Colombo G (1965) Rotational Period of the Planet Mercury. *Nature* 208(5010):575–575, 10.1038/208575a0
- Duxbury TC (1989) The figure of PHOBOS. *Icarus* 78:169–180
- Duxbury TC (2017) on HRSC team meeting, Münster Apr. 2017
- Duxbury TC, Hoffmann H, Roatsch T, Oberst J, Behnke T, Schwarz G (2011) Mars Express Super Resolution Channel Image Restoration and Geometric Properties. Tech. rep., School of Physics, Astronomy and Computational Sciences, George Mason University, Fairfax, VA USA
- Gehrels T (1967) Minor planets. I. The rotation of Vesta. *Astronomical Journal* 72:929, DOI 10.1086/110364
- Giese B, Hussmann H, Roatsch T, Helfenstein P, Thomas PC, Neukum G (2011) Enceladus: Evidence for librations forced by Dione. EPSC Abstracts Vol. 6, EPSC-DPS2011-976
- Jacobson RA (2008) Ephemerides of the Martian Satellites MAR080. IOM 343R-08-006, JPL
- Jacobson RA (2010) The orbits and masses of the martian satellites and the libration of Phobos. *The Astronomical Journal* 139:668–679
- Jacobson RA (2017) The Orientations of the Martian Satellites from a Fit to Ephemeris MAR097 Revised. JPL - IOM 392R-17-007
- Jacobson RA, Lainey V (2014) Martian satellite orbits and ephemerides. *Planetary and Space Science* 102:35–44
- Jaumann R, Neukum G, Behnke T, Duxbury TC, Eichtenopf K, Flohrer J, Gasselt Sv, Giese B, Gwinner K, Hauber E, Hoffmann H, Hoffmeister A, Köhler U, Matz KD, McCord TB, Mertens V, Oberst J, Pischel R, Reiss D, Ress E, Roatsch T, Saiger P, Scholten F, Schwarz G, Stephan K, Wählisch M (2007) The high-resolution stereo camera (HRSC) experiment on Mars Express: Instrument aspects and experiment conduct from interplanetary cruise through the nominal mission. *Planetary and Space Science* 55:928–952
- Klaasen KP, Thorpe TE, Morabito LA (1977) Inflight performance of the viking visual imaging subsystem. *Applied Optics* 16(12):3158–3170
- Konopliv AS, Sjogren WL (1995) The JPL Mars gravity field, Mars50c, based upon Viking and Mariner 9 Doppler tracking data. NASA STI/Recon Technical Report N 95
- Konopliv AS, Asmar SW, Park RS, Bills BG, Zuber MT, et al (2014) The Vesta gravity field, spin pole and rotation period, landmark positions, and ephemeris from the Dawn tracking and optical data. *Icarus* 240:103–117
- Mastrodemos N, Rush B, Vaughan D, Owen W (2001) Optical navigation for Dawn at Vesta. AAS Paper 11-222
- Oberst J, Schwarz G, Behnke T, Hoffmann H, Matz KD, Neukum G, et al (2008) The imaging performance of the SRC on Mars Express. *Planetary and Space Science* 56:473–491
- Oberst J, Zubarev A, Nadezhdina I, Shishkina L, Rambaux N (2014) The phobos geodetic control point network and rotation model. *Planetary and Space Science* 102:45–50
- Owen WM, Jr, Wang TC, Harch A, Bell M, Peterson C (2001) NEAR optical navigation at Eros. *Advances in the Astronautical Sciences* (D B Spencer, C C Seybold, A K Misra, and R J Lisowski, Eds) 109:1075–1090
- Pasewaldt A, Oberst J, Willner K, Beisembin B, Hoffmann H, Matz KD, Roatsch T, Michael G, Cardesin-Moinelo A, Zubarev AE (2015) Astrometric observations

- of Phobos with the SRC on Mars Express. *A&A* 580:A28
- Peale SJ, Gold T (1965) Rotation of the Planet Mercury. *Nature* 206(4990):1240–1241, 10.1038/2061240b0
- Pischel R, Zegers T (2009) Mars Express: The Scientific Investigations, ESA SP-1291, chap Mars Express Science Planning and Operations, pp 249–256
- Pravec P, Harris AW, Michalowski T (2002) Asteroid Rotations; in Book Asteroids III, Ed. Bottke, Jr., W. F. and Cellino, A. and Paolicchi, P. and Binzel, R. P., Univ. of Arizona Press, pp 113–122
- Preusker F, Scholten F, Matz KD, Roatsch T, Willner K, Hviid SF, Vincent JB, et al (2015) Shape model, reference system definition, and cartographic mapping standards for comet 67P/Churyumov-Gerasimenko - Stereophotogrammetric analysis of Rosetta/OSIRIS image data. *A&A* 583:A33, DOI 10.1051/0004-6361/201526349
- Rambaux N, Castillo-Rogez JC, Le Maistre S, Rosenblatt P (2012) Rotational motion of Phobos. *Astronomy & Astrophysics* 548:A14
- Rosenblatt P, Lainey V, Maistre SL, Marty J, Husler Bea (2008) Accurate mars express orbits to improve the determination of the mass and ephemeris of the martian moons. *Planetary and Space Science* 56(7):1043 – 1053, DOI <https://doi.org/10.1016/j.pss.2008.02.004>
- Stark A, Willner K, Burmeister S, Oberst J (2017) Geodetic Framework for Martian Satellite Exploration I: Reference rotation models. EPSC Abstracts Vol. 11, EPSC2017-868-1
- Tajeddine R, Rambaux N, Lainey V, Charnoz S, Richard A, Rivoldini A, Noyelles B (2014) Constraints on Mimas' interior from Cassini ISS libration measurements. *Science* 346:322–324
- Thomas PC, Tajeddine R, Tiscareno MS, Burns JA, Joseph J, Loredó TJ, Helfenstein P, Porco C (2016) Enceladus's measured physical libration requires a global subsurface ocean. *ICARUS* 264:37–47
- Tiscareno MS, Thomas PC, Burns Ja (2009) The rotation of Janus and Epimetheus. *Icarus* 204:254–261
- Williams JG, Konopliv AS, Boggs DH, Park RS, Yuan DN, Lemoine FG, Goossens S, Mazarico E, Nimmo F, Weber RC, Asmar SW, Melosh HJ, Neumann GA, Phillips RJ, Smith DE, Solomon SC, Watkins MM, Wieczorek MA, Andrews-Hanna JC, Head JW, Kiefer WS, Matsuyama I, McGovern PJ, Taylor GJ, Zuber MT (2014) Lunar interior properties from the GRAIL mission. *Journal of Geophysical Research: Planets* 119(7):2013JE004559
- Willner K (2009) The Martian Moon Phobos – A Geodetic Analysis of its Motion, Orientation, Shape, and Physical Parameters. Phd thesis, Technische Universität Berlin, DOI 10.14279/depositonce-2338
- Willner K, Oberst J, Hussmann H, Giese B, Hoffmann H, Matz KD, Roatsch T, Duxbury T (2010) Phobos control point network, rotation, and shape. *Earth and Planetary Science Letters* 294:541–546
- Witasse O, Duxbury T, Chicarro A, Altobelli N, Andert T, Aronica A, Barabash S, Zegers T, et al (2014) Mars Express investigations of Phobos and Deimos. *Planetary and Space Science* 102:18–34
- Zeitler W, Oberst J (1999) The Mars Pathfinder landing site and the Viking control point network. *Journal of Geophysical Research (Planets)* 104:8935–8942